coatings

MDPI

Article

Reduction of Surface Residual Lithium Compounds for Single-Crystal $LiNi_{0.6}Mn_{0.2}Co_{0.2}O_2$ via Al_2O_3 Atomic Layer Deposition and Post-Annealing

Jiawei Li [1], Junren Xiang [1], Ge Yi [1], Yuanting Tang [2], Huachen Shao [1], Xiao Liu [1,*], Bin Shan [2] and Rong Chen [1,*]

[1] State Key Laboratory of Digital Manufacturing Equipment and Technology, School of Mechanical Science and Engineering, Huazhong University of Science and Technology, Wuhan 430074, China; jiaweili@hust.edu.cn (J.L.); junrenxiang@hust.edu.cn (J.X.); geyigeyi@hust.edu.cn (G.Y.); shaohuachen@hust.edu.cn (H.S.)

[2] State Key Laboratory of Materials Processing and Die and Mould Technology, School of Materials Science and Engineering, Huazhong University of Science and Technology, Wuhan 430074, China; yuanting015@163.com (Y.T.); bshan@mail.hust.edu.cn (B.S.)

* Correspondence: xiaoliu@hust.edu.cn (X.L.); rongchen@mail.hust.edu.cn (R.C.)

Abstract: Surface residual lithium compounds of Ni-rich cathodes are tremendous obstacles to electrochemical performance due to blocking ion/electron transfer and arousing surface instability. Herein, ultrathin and uniform Al_2O_3 coating via atomic layer deposition (ALD) coupled with the post-annealing process is reported to reduce residual lithium compounds on single-crystal $LiNi_{0.6}Mn_{0.2}Co_{0.2}O_2$ (NCM622). Surface composition characterizations indicate that LiOH is obviously reduced after Al_2O_3 growth on NCM622. Subsequent post-annealing treatment causes the consumption of Li_2CO_3 along with the diffusion of Al atoms into the surface layer of NCM622. The NCM622 modified by Al_2O_3 coating and post-annealing exhibits excellent cycling stability, the capacity retention of which reaches 92.2% after 300 cycles at 1 C, much higher than that of pristine NCM622 (34.8%). Reduced residual lithium compounds on NCM622 can greatly decrease the formation of LiF and the degree of Li^+/Ni^{2+} cation mixing after discharge–charge cycling, which is the key to the improvement of cycling stability.

Keywords: $LiNi_{0.6}Mn_{0.2}Co_{0.2}O_2$; cycling stability; residual lithium compounds; atomic layer deposition; post-annealing

check for updates

Citation: Li, J.; Xiang, J.; Yi, G.; Tang, Y.; Shao, H.; Liu, X.; Shan, B.; Chen, R. Reduction of Surface Residual Lithium Compounds for Single-Crystal $LiNi_{0.6}Mn_{0.2}Co_{0.2}O_2$ via Al_2O_3 Atomic Layer Deposition and Post-Annealing. *Coatings* **2022**, *12*, 84. https://doi.org/10.3390/coatings12010084

Academic Editor: Alessio Lamperti

Received: 14 December 2021
Accepted: 6 January 2022
Published: 12 January 2022

1. Introduction

Ni-rich cathodes ($LiNi_xCo_yMn_{1-x-y}O_2$, $x \geq 0.6$, NCM) have attracted much attention for powering lithium-ion batteries for electric vehicles due to the high energy density and relatively low cost [1,2]. However, serious interfacial issues between NCM and the electrolytes limit the cycling life and safety for applications due to the structural and electrochemical instability of the NCM surface [3–5]. Although single-crystal NCM usually exhibits good structural stability, it suffers from serious side reactions between surface residual lithium compounds (LiOH and Li_2CO_3) and the electrolyte during discharge–charge cycling. The surface residual lithium compounds can react with $LiPF_6$ in the electrolyte to form LiF on the surface of NCM and produce CO_2, which increases the interfacial resistance and battery internal pressure, and leads to heat generation [6–9]. Surface residual lithium compounds can reduce the lifespan of batteries and induce serious safety issues.

Since excess lithium precursor is needed to suppress Li^+/Ni^{2+} cation mixing during the NCM preparation process, it is difficult to avoid the formation of residual lithium compounds when the surface Li^+ cations are exposed to air containing moisture and CO_2 [10–12]. In order to reduce surface residual lithium compounds of NCM materials, washing with water is a widely used method in industrial manufacturing. However, after the washing process, surface residual lithium compounds are usually more rapidly formed when NCM materials are exposed to air again [7,13]. The control of solid-to-water ratio and washing time cannot prevent Li^+ leaching from NCM, which leads to capacity loss [14]. Hence, post-annealing is put forward to repair the NCM surface after washing with water [15]. Recently, surface chemical reactions have been utilized to reduce residual lithium compounds, which can be classified into liquid-solid, solid-solid, and gas-solid reactions. For liquid-solid reactions, some acids such as phosphoric acid, boracic acid, and oxalic acid have been applied to neutralize alkaline residual lithium compounds [16–18]. For instance, phosphoric acid can not only react with residual lithium compounds, but also form a Li_3PO_4 coating, which can facilitate Li^+ diffusion and improve the cycle stability [16]. Unlike liquid-liquid reactions, solid-solid reactions activated at high temperatures can avoid NCM materials' exposure to water. A lithium-containing coating can form after the post-annealing of NCM materials is mixed with cobalt hydroxide or phosphate composite [19–21]. Based on sufficient gas-solid contact, gas-solid reactions have also been performed to reduce residual lithium compounds. The sublimated gas-phase S can react with residual lithium compounds on the surface of NCM particles and form $Li_xS_yO_z$ protective layers [22]. SO_2 has been introduced into the reactor during the cooling process of NCM synthesis process. Li_2SO_4 coating is formed due to the reactions between LiOH and SO_2, which effectively enhances the cycling stability of NCM [23]. Based on sequential and self-limiting surface gas-solid reactions, atomic layer deposition (ALD) become a widely used method to prepare ultrathin and conformal coating [24,25]. Various materials (such as Al_2O_3, ZrO_2, TiO_2 and ZnO) have been reported to coat NCM [26–30]. Although the enhanced cycling stability of NCM materials is commonly attributed to the protection of the NCM surface, we believe that the behavior of surface residual lithium compounds during ALD process is an important factor to affect the surface reactions between the cathode and the electrolyte.

In this work, a commonly reported Al_2O_3 coating has been prepared to investigate the behavior of residual lithium compounds of single-crystal $LiNi_{0.6}Mn_{0.2}Co_{0.2}O_2$ (NCM622) during ALD process. The morphology and surface composition results indicate that ultrathin Al_2O_3 is coated on NCM622 particles and the Al_2O_3 ALD process can reduce residual LiOH. By performing the post-annealing process after Al_2O_3 ALD, the residual Li_2CO_3 on NCM622 can be reduced with Al diffusing into NCM particles and forming surface Al doping. The reduced residual lithium compounds by Al_2O_3 coating coupled with post-annealing can greatly improve the cycling stability of NCM622 cathodes by decreasing the formation of LiF and the degree of Li^+/Ni^{2+} cation mixing during charge–discharge cycling.

2. Materials and Methods

2.1. Materials Preparation

Al_2O_3 coating was prepared directly on commercially available NCM622 particles (Ningbo Gaosi New Energy Technology Co., Ltd., Ningbo, China) using a home-made fluidized bed ALD reactor. Al_2O_3 was deposited at 150 °C using $Al(CH_3)_3$ and H_2O as precursors. In a typical Al_2O_3 ALD cycle, 120 s $Al(CH_3)_3$ pulse, 180 s N_2 purge, 120 s H_2O pulse, and 180 s N_2 purge were alternately operated. The NCM622 particles were coated with Al_2O_3 in different numbers of ALD cycles. For example, 0, 2, 4, and 8 ALD cycles of Al_2O_3 on NCM622 particles were referred to as bare, 2AL, 4AL, and 8AL NCM622 particles. After the Al_2O_3 ALD process, the samples were subsequently annealed at 500 °C in air for 3 h, which were referred to as 2AL-A, 4AL-A, and 8AL-A NCM622 particles.

2.2. Materials Characterizations

The crystalline structures of NCM622 samples were characterized by a PANalytical X'Pert (PANalytical B.V., Malvern, UK) X-ray diffractometer (XRD) with a Cu Ka radiation (λ = 1.5406 Å). The morphologies of NCM622 samples were characterized using a Quanta650 FEG (FEI Instrument, Tokyo, Japan) scanning electron microscope (SEM) and a JEM F200 (JEOL instrument, Tokyo, Japan) transmission electron microscope (TEM) with an acceleration voltage of 200 kV. The composition analysis was performed by a JEM F200 (JEOL instrument, Tokyo, Japan) scanning transmission electron microscope (STEM) integrated with energy-dispersive X-ray spectroscopy (EDS). The XPS (X-ray photoelectron spectroscopy) spectra were recorded with an AXIS-ULTRA X-ray photoelectron spectroscopy (Shimadzu-Kratos Co., Manchester, UK). All spectra were aligned by calibrating the C 1s peak at 285 eV. High-resolution XPS spectra were collected in the regions around Al 2p, O 1s, Li 1s, and F 1s. For pH measurements, 50 mg of NCM622 particles were put into 20 mL of deionized water with magnetic stirring for 10 min to make the slurry. The pH of the slurry was measured using a S210-K pH meter (Mettler Toledo, Zurich, Switzerland). The electronic conductivity was calculated based on the powder resistance measured via a multimeter at a certain pressure. In details, 100 mg of NCM622 sample was pressed into a tubular mold with the diameter of 8 mm under the pressure of 20 MPa.

2.3. Electrochemical Measurements

NCM622, carbon black, and polyvinylidene fluoride (PVDF) with a weight ratio of 8:1:1 were added into N-methyl pyrrolidine (NMP) to prepare the slurries. The NCM622 cathode laminates were made by casting the slurries on carbon-coated Al foils and drying them in a vacuum oven (Yiheng, Shanghai, China) at 120 °C overnight. The loading of NCM622 was about 2.6–3.4 mg/cm^2. The electrolyte contained 1 M $LiPF_6$ dissolved in EC/EMC/DMC (1:1:1 by volume). Celgard 2400 (Celgard, Charlotte, NC, USA) was used as the separator. The coin cells (CR2025) were assembled in an argon-filled MB-Unilab glovebox (Mbraun, Stratham, Germany) with Li foil as the counter electrode. Charge-discharge tests were conducted on a Land CT3002A battery tester (Land, Wuhan, China) at 1 C (180 mA/g) with a voltage range from 3.0 to 4.5 V at 20 °C. Electrochemical impedance spectra (EIS) measurements were conducted using an Autolab PGSTAT302N electrochemical station (Metrohm AG, Herisau, Switzerland) over the frequency range of 0.01 Hz to 100 kHz with an amplitude perturbation of ±5 mV.

3. Results

Crystal structures of bare, 2AL, and 2AL-A NCM622 particles are shown in Figure 1a. All samples show well-separated (006)/(012) peaks and (108)/(110) peaks, implying the typical α-$NaFeO_2$ layered structure. No extra peaks and no peak shifts are detected in the XRD patterns of 2AL and 2AL-A samples, indicating that the ALD and post-annealing processes have no influence on the crystal structures of substrate materials. The XRD patterns of 4AL, 8AL, 4AL-A, and 8AL-A shown in Figure S1 also indicate no crystal structure change on NCM622 particles. The morphologies of bare and coated NCM622 particles are analyzed by SEM. As shown in Figure 1b,c, the bare NCM622 particles show polygonal shapes with the size of 2–3 µm. As the SEM images shown in Figure 1d,e, the morphologies of NCM622 particles show no change after the ALD coating and post-annealing treatment. Figure S2 also shows the morphologies of NCM622 particles coated by more ALD cycles keep the same as the bare NCM622 particles.

TEM and EDS were performed to characterize the surface morphologies and compositions of 2AL and 2AL-A NCM622 particles. As shown in Figure 2a, the edges of the 2AL NCM622 particles are smooth. As the high-resolution TEM (HR-TEM) image shown in Figure 2b, the measured lattice spacing is 0.472 nm, which is assigned to the NCM622 (003) plane. Since the theoretical thickness of 2 ALD cycles of Al_2O_3 is about 2–3 Å, no obvious Al_2O_3 coating can be observed [31–34]. In order to identify the existence of Al_2O_3 coating, EDS analysis in Figure 2c shows a clear Al signal with an atomic concentration of 5.73% at the edge location (P1) of NCM622 particles. In comparison, a weak Al signal with an atomic concentration of 0.58% is detected at the interior location (P2) due to lots of transition metal signals of bulk NCM622. Furthermore, 20 ALD cycles of Al_2O_3 have been prepared on NCM622 particles with the same ALD process. As shown in Figure 2d, 20AL

NCM622 particles also exhibit smooth edges. As the HR-TEM image shown in Figure 2e, 2.6 nm amorphous Al_2O_3 coating can be clearly observed and the corresponding growth rate is calculated as 1.3 Å/cycle, which agrees well with previous reports [31–34]. EDS analysis in Figure 2f shows a strong Al signal with a much higher atomic concentration of 20AL NCM622 particles than that of 2AL NCM622 particles, which is attributed to a thicker Al_2O_3 coating. As shown in Figure 2g,h, it is also difficult to observe the Al_2O_3 coating on 2AL-A NCM622 particles. The lattice spacing of 0.245 nm is assigned to the NCM622 (101) plane. As shown in Figure 2i, the EDS results also show the Al signal on the surface of 2AL-A NCM622 particles. The decreased atomic concentration of Al can be attributed to Al atoms diffusing into the bulk of NCM622 particles after post-annealing.

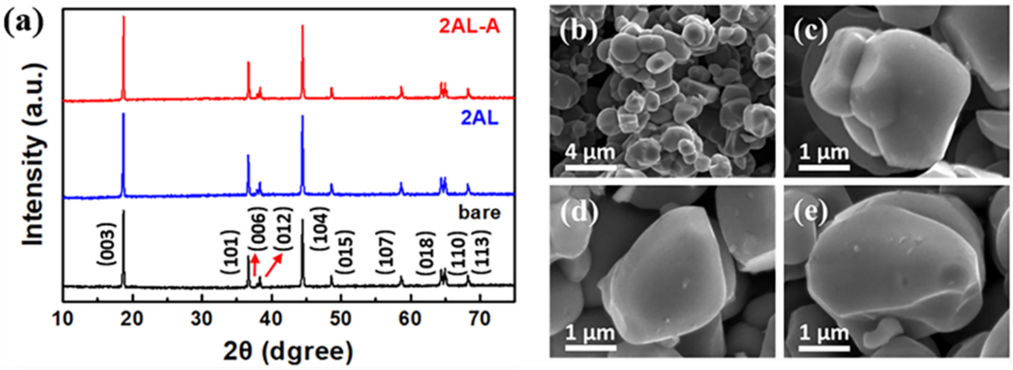

Figure 1. (**a**) XRD patterns of bare, 2AL, and 2AL-A NCM622 particles (the red arrows indicate diffraction peaks at 2theta of 37.9° and 38.3°). SEM images of (**b**,**c**) bare, (**d**) 2AL, and (**e**) 2AL-A NCM622 particles.

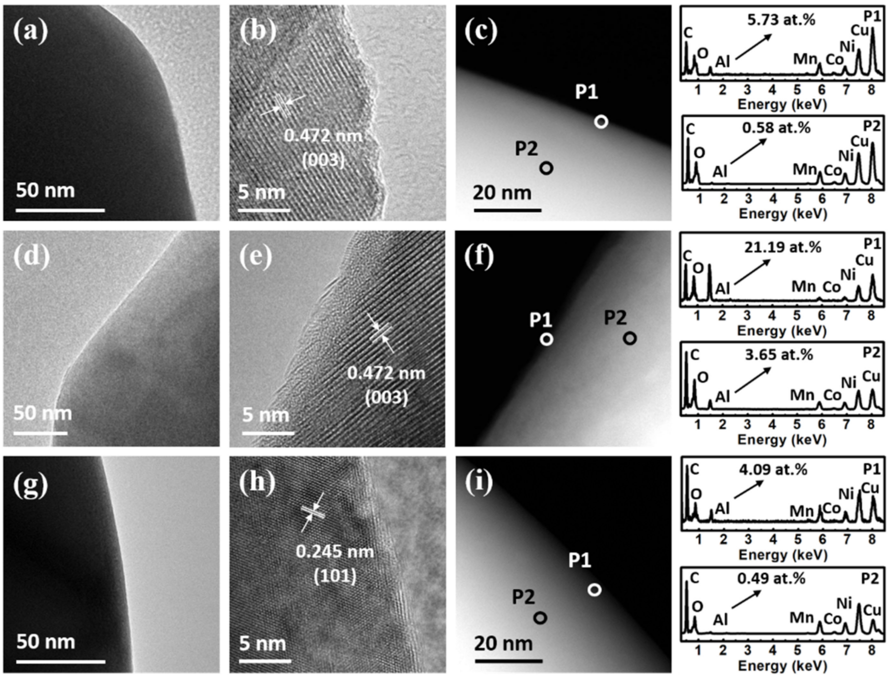

Figure 2. (**a**) TEM, (**b**) HR-TEM, (**c**) STEM images of 2AL NCM622 particles. (**d**) TEM, (**e**) HR-TEM, (**f**) STEM images of 20AL NCM622 particles. (**g**) TEM, (**h**) HR-TEM, (**i**) STEM images of 2AL-A NCM622 particles. The EDS spectra of edge (P1) and interior (P2) locations are shown at the right of corresponding STEM images.

XPS characterization has been performed to investigate the composition of Al_2O_3 coating. As shown in Figure 3a, 2AL NCM622 shows the Al 2p peak at 74.5 eV. After post-annealing, the Al 2p peak of 2AL-A NCM622 shifts to lower binding energies at 73.6 eV, which illustrates the formation of surface Al doping and $LiAlO_2$ [35–37]. As the ALD cycles increase, the binding energies of Al 2p for 4AL NCM622 and 8AL NCM622 have no change compared with 2AL NCM622, whereas the intensity of Al 2p peak increases when taking Ni 3p peak as a reference. In order to further investigate the Al contents on the surface of NCM622 particles, the Al/Ni atomic ratios are shown in Figure 3b. The Al/Ni atomic ratios of 4AL NCM622 and 8AL NCM622 increase to 3.67 and 6.45 compared with that of 2AL NCM622, which is attributed to the increased thickness of Al_2O_3 coating. The Al/Ni atomic ratio of 2AL-A NCM622 particles shows a slight decrease, which indicates that the post-annealing treatment leads to Al atoms diffusing into NCM622 particles. As the O 1s XPS spectrum shows in Figure 3c, two peaks at 529.5 and 532.1 eV can be observed, which can be assigned to lattice oxygen in NCM622 and surface oxygen in Li_2CO_3, LiOH, and Al_2O_3, respectively [38,39]. The intensities of surface oxygen species increase with the increase in Al_2O_3 ALD cycles. The surface oxygen intensity of 2AL-A NCM622 shows a noteworthy decline compared with that of 2AL NCM622 and bare NCM622, which can be attributed to the transformation of Al_2O_3 coating into Al doping on the surface and the consumption of surface Li_2CO_3.

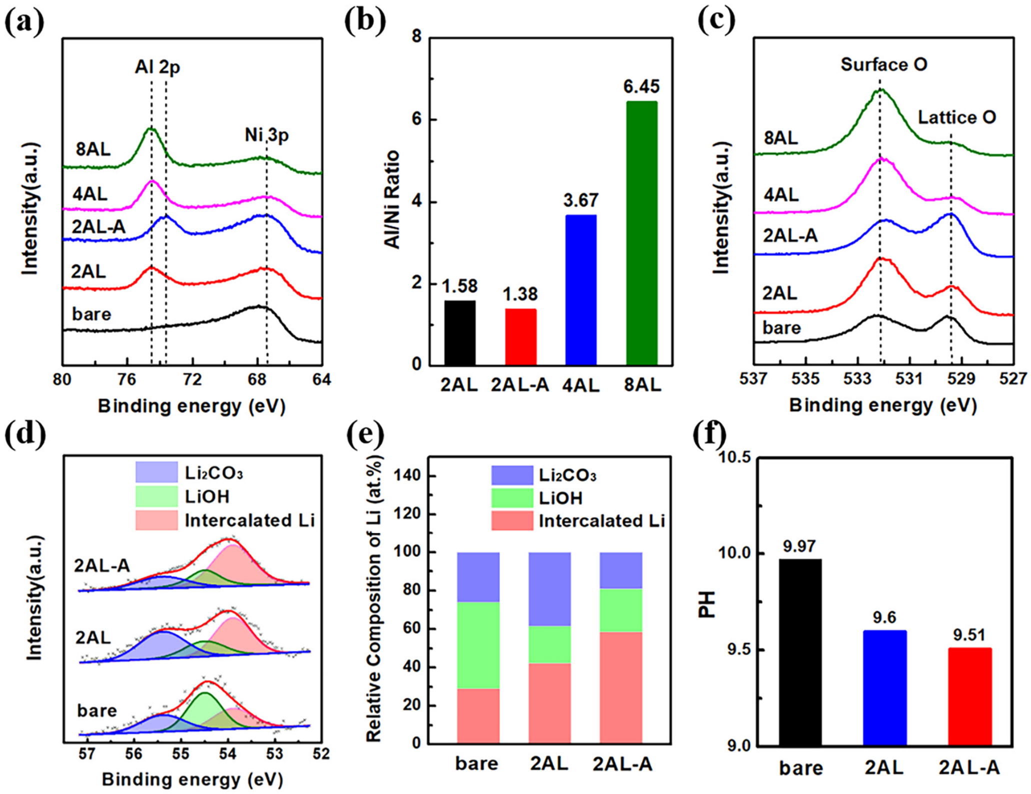

Figure 3. (**a**) Al 2p and Ni 3p XPS spectra, (**b**) Al/Ni ratios and (**c**) O 1s XPS spectra of bare, 2AL, 2AL-A, 4AL and 8AL NCM622 particles. (**d**) Li 1s XPS spectra, (**e**) the relative concentrations of surface Li species and (**f**) pH values of bare, 2AL, 2AL-A NCM622 particles.

Li 1s XPS spectra have been collected to explore the influence of ALD on surface residual lithium compounds. As shown in Figure 3d, three peaks at 53.9, 54.5 and 55.4 eV in Li 1s XPS spectra can be observed, which can be assigned to intercalated lithium, LiOH and Li_2CO_3, respectively [14,40,41]. The relative concentrations of intercalated lithium, LiOH and Li_2CO_3 are shown in Figure 3e. After 2 ALD cycles of Al_2O_3, the relative concentration of LiOH decreases, which can be attributed to the reactions between surface LiOH and

$Al(CH_3)_3$ precursor during the Al_2O_3 ALD process [42,43]. After the post-annealing process, the relative concentration of Li_2CO_3 decreases, which can be attributed to the consumption of surface Li_2CO_3 [37]. Furthermore, the pH value has been measured to check the content of residual lithium compounds on the surface of NCM622 particles. As shown in Figure 3f, the pH of the slurry consisting of 2AL NCM622 particles and deionized water shows an obvious decrease. Moreover, the pH of the slurry is further reduced after post-annealing. The pH results are consistent with XPS results.

The electrochemical performance of NCM622 cathodes after ALD coating and post-annealing treatment has been evaluated in coin cells with a lithium-metal anode. As the initial discharge curves shown in Figure 4a,b, the initial discharge capacity decreases with the increasing Al_2O_3 ALD cycles, which can be related to the increased polarization voltage (Figure S3). With the decrease in polarization voltage, the post-annealing treatment can slightly increase the initial discharge capacity for NCM622 cathodes with the same ALD cycles of Al_2O_3. The coulombic efficiency of the 2AL-A NCM622 cathode can reach 82.94%, which is close to that of the bare NCM622 cathode (83.41%). The rate capability in Figure 4c,d also shows the same tendency as the initial discharge capacity for NCM622 cathodes with Al_2O_3 coating, which can be attributed to the decreased electronic conductivity (Figure S4). Nevertheless, the discharge capacity of the 2Al-A NCM622 cathode can be close to that of the bare NCM622 cathode at the 0.5 and 1 C rates. The discharge capacity of the 2AL-A NCM622 cathode is larger than that of the 2AL NCM622 cathode at 2C. Figure 4e shows the cycling performance of bare, 2AL and 2AL-A NCM622 cathodes at 1 C. The bare NCM622 cathode suffers from obvious electrochemical performance degradation with the capacity retention of 34.8% and the final capacity of 48.5 mAh/g after 300 charge-discharge cycles. The post-annealing treatment has no evident influence on the rate performance and cycling stability of bare NCM622 cathode (Figure S5). Although the 2AL NCM622 cathode shows lower initial capacity, it exhibits higher capacity retention of 86.1% with the final capacity of 111.0 mAh/g. Compared with the bare and the 2AL NCM622 cathode, the 2AL-A NCM622 cathode exhibits the best capacity retention (92.2%) and the highest final capacity (128.4 mAh/g). To the best of our knowledge, the NCM622 cathode modified by Al_2O_3 ALD and post-annealing shows outstanding capacity retention compared with NCM622 cathodes modified by other methods reported in literature (Table S1) [17,44–50]. It shows only 0.026% capacity loss per cycle, which is lower than most NCM622 cathodes modified by other methods.

To understand the electrochemical behavior of the bare, 2AL, and 2AL-A cathodes during cycling, the differential capacity plots are analyzed (Figure S6). The detailed potential differences have been presented in Figure 5a, which are 0.13 V, 0.16 V and 0.15 V for the bare, 2AL and 2AL-A NCM622 cathodes at the second charge–discharge cycle, respectively. The potential differences increase to 0.94, 0.45 and 0.25 V for the bare, 2AL and 2AL-A NCM622 cathodes at 300th charge-discharge cycle. The bare NCM622 cathode shows the highest potential shift of 0.81 V, whereas the 2AL and 2AL-A NCM622 cathodes show much lower potential shift of 0.29 and 0.10 V, which indicates that 2 ALD cycles of Al_2O_3 and post-annealing can decrease the polarization after cycling. Furthermore, the 2AL and 2AL-A NCM622 cathodes can keep the intensity of redox peaks after cycling compared with the bare NCM622 cathode (Figure S6), indicating the Al_2O_3 coating and post-annealing can improve the electrochemical stability of the NCM622 cathode.

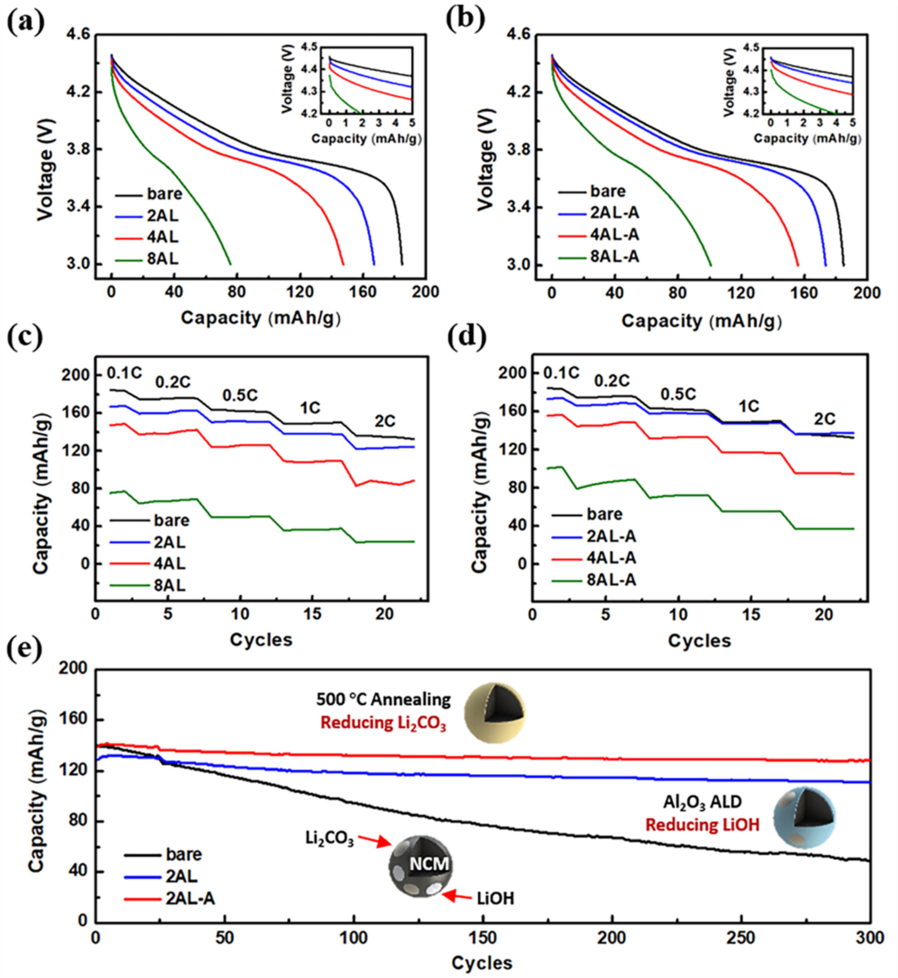

Figure 4. Initial discharge curves of (**a**) bare, 2AL, 4AL and 8AL NCM622 and (**b**) bare, 2AL-A, 4AL-A and 8AL-A NCM622. Rate capability of (**c**) bare and 2AL, 4AL and 8AL NCM622, and (**d**) bare, 2AL-A, 4AL-A, and 8AL-A NCM622. (**e**) Cycling stability of bare, 2AL, and 2AL-A NCM622.

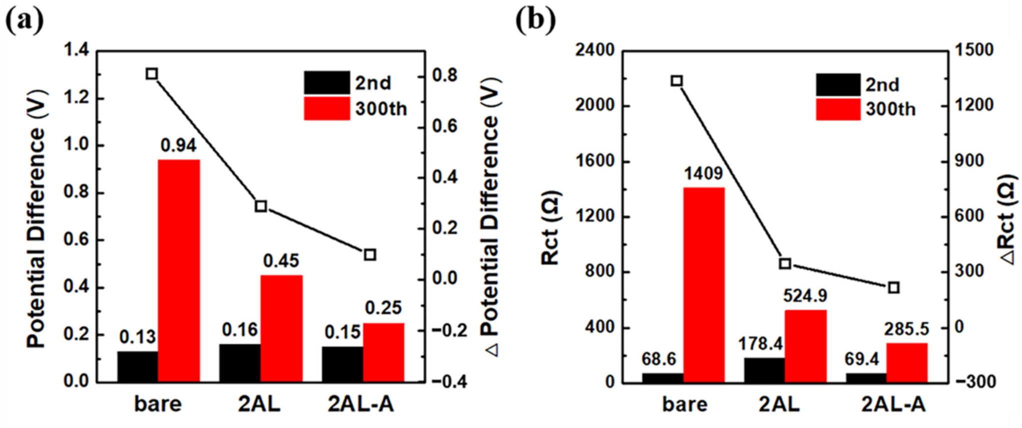

Figure 5. (**a**) Potential differences of redox peaks of bare, 2AL and 2AL-A NCM622 cathodes at the 2nd and 300th charge-discharge cycles. (**b**) Charge transfer resistances of bare, 2AL and 2AL-A NCM622 cathodes after the 2nd and 300th charge-discharge cycles at a charged state of 4.5 V.

To investigate the effect of Al_2O_3 ALD and post-annealing on the Li^+ transport behavior, electrochemical impedance spectra (EIS) are measured after the 2nd and 300th charge–discharge cycles at a charged state of 4.5V (Figure S7). The resistance of charge transfer (R_{ct}) shows obvious differences during cycling. Figure 5b shows the fitting results of R_{ct}. After the second charge–discharge cycle, the 2AL NCM622 cathode shows higher R_{ct} than the bare NCM622 cathode, which indicates Al_2O_3 coating limits the transfer of Li^+ at the interface between the NCM622 particles and the electrolyte. The R_{ct} of 2AL NCM622 is reduced after post-annealing, indicating the resistance decrease in Li^+. After the 300th charge–discharge cycle, the bare NCM622 cathode shows the largest increment of R_{ct}, which indicates the rapid growth of the Li^+ barrier layer on the bare NCM622 particles. Conversely, the 2AL NCM622 and 2AL-A NCM622 cathodes show the lower increment of R_{ct}. The most stable interface of the 2AL-A NCM622 cathode is responsible for the highest capacity retention.

Figure 6 shows the SEM images of the NMC622 cathodes from the coin cells before and after cycling. As shown in Figure 6a–c, the spotty species can be observed on the surface, which belong to cathode electrolyte interface (CEI) layers on NCM622 particles [51]. Many spotty species can be observed on the 2AL NCM622 particles, which are responsible for the high polarization and low initial coulombic efficiency. As shown in Figure 6d–f, the thicker spotty layer can be clearly observed on the bare NCM622 particles after cycling, which reflects the rapid growth of CEI layers. In comparison, the 2AL and 2AL-A NCM622 particles show fewer spotty species, indicating fewer side reactions on the surface during the cycling process. To further explore the interfacial stability between the NCM622 particles and the electrolyte, XPS characterizations were carried out to investigate the surface F containing species. As shown in Figure 6g, the F 1s peaks at 685.0 eV and 688.6 eV can be assigned to LiF and PVDF. An obvious LiF signal has been detected for bare NCM622 cathodes, which is a significant source of sluggish Li^+ transport kinetics and leads to capacity fading. 2AL-A NCM622 cathode shows the minimum LiF on the surface, indicating Al_2O_3 ALD and post-annealing effectively inhibit side reactions. Moreover, XRD characterizations were carried out to investigate the crystal structure changes after cycling. Compared with the XRD patterns of pristine (Figure S8) and cycled NCM622 cathodes (Figure 6h), the intensity of all peaks decreases without extra peaks and peak shift, which is attributed to the formation of amorphous CEI layers on NCM622 particles. The ratios of the (003) peak intensity to the (104) peak intensity of pristine and cycled bare, 2AL, and 2AL-A NCM622 cathodes are 1.15, 1.12, 1.11 and 0.51, 0.59, 0.61, respectively. The 2AL-A NCM622 cathode shows the lowest change of the ratios of the (003) peak intensity to the (104) peak intensity after cycling, which reflects the lowest Li^+/Ni^{2+} cation mixing during cycling. These results show Al_2O_3 coating and post-annealing reduce the consumptions and inhibitions to active Li^+ during cycling, which is the key to high capacity retention.

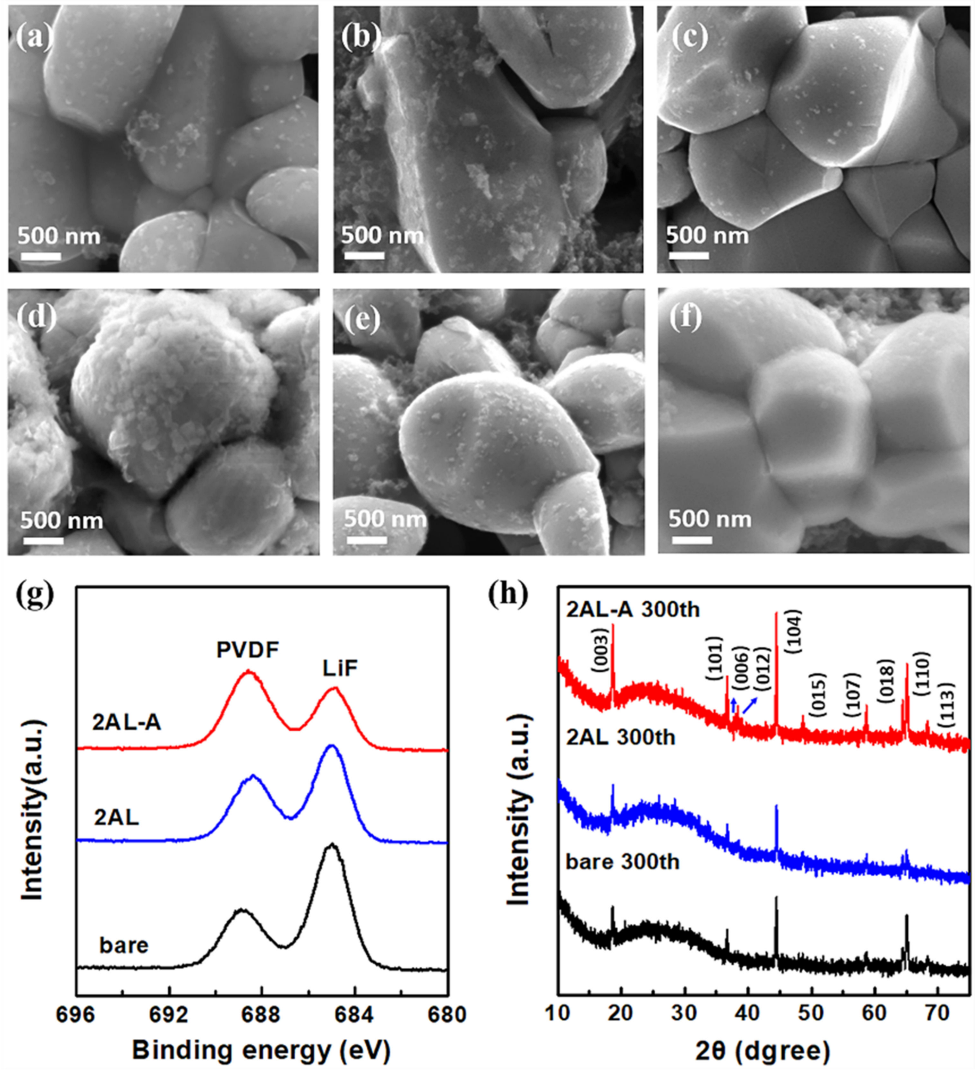

Figure 6. SEM images of (**a**) bare, (**b**) 2AL and (**c**) 2AL-A NCM622 cathodes recovered from cells before cycling. SEM images of (**d**) bare, (**e**) 2AL, and (**f**) 2AL-A NCM622 cathodes recovered from cells after cycling. (**g**) F 1s XPS spectra and (**h**) XRD patterns of bare, 2AL and 2AL-A NCM622 cathodes after cycling (the blue arrows indicate diffraction peaks at 2theta of 37.9° and 38.3°).

4. Conclusions

In summary, ultrathin and uniform Al_2O_3 coating via ALD coupled with the post-annealing process has been performed to reduce the surface residual lithium compounds of NCM622. LiOH species can be reduced during the ALD process, whereas Li_2CO_3 species can be reduced with the formation of surface Al doping after the post-annealing treatment. The reduced residual lithium compounds by Al_2O_3 coating and surface Al doping greatly improve the cycling stability of NCM622 cathodes. The reduced surface lithium compounds can decrease LiF deposition and Li^+/Ni^{2+} cation mixing after charge-discharge cycling, which keeps the interfacial conductivity of Li ions. This work sheds light on the behavior of surface lithium compounds during ALD coating, which is important for the stability enhancement of Ni-rich NCM cathodes.

Supplementary Materials: The following supporting information can be downloaded at: https://www.mdpi.com/article/10.3390/coatings12010084/s1, Figure S1: XRD patterns of bare, 4AL, 8AL, 4AL-A and 8AL-A NCM622 particles (the red arrows indicate diffraction peaks at 2theta of 37.9° and 38.3°). All samples show well-separated (006)/(012) peaks and (108)/(110) peaks, implying the typical α-NaFeO2 layered structure. No extra peaks and no peak shift are detected in the XRD patterns of

4AL, 8AL, 4AL-A and 8AL-A samples, indicating that the ALD and post-annealing processes have no influence on the crystal structure of substrate materials; Figure S2: SEM images of (a) 4AL, (b) 8AL, (c) 4AL-A and (d) 8AL-A NCM622 particles. No obvious changes are observed in the morphologies after the ALD process or post-annealing; Figure S3: (a) Polarization voltages at the initial discharge stage and (b) initial coulombic efficiencies of bare, coated and annealed NCM622 cathodes. The post-annealing relieves the increment of polarization voltages and the decline of coulombic efficiencies; Figure S4: Electronic conductivities of bare, 2AL, and 2AL-A NCM622 particles. The electronic conductivity decreases after the Al2O3 ALD process and post-annealing process; Figure S5: (a) Rate capability and (b) cycling stability of bare and bare-A NCM622 cathodes. These two cathodes show similar rate capability and cycling stability; Figure S6: Differential capacity versus voltage profiles of (a) bare, (b) 2AL, and (c) 2AL-A NCM622 cathodes at the 2nd and 300th charge-discharge cycles. The 2AL-A NCM622 cathode well keeps the potential difference and intensity of redox peaks after cycles compared to others; Figure S7: Electrochemical impedance spectra (EIS) of bare, 2AL, and 2AL-A NCM622 cathodes after the 2nd charge-discharge cycle (a) and the 300th charge-discharge cycle (b) at a charged state of 4.5V. The 2AL-A NCM622 cathode shows the lowest increment of Rct compared to others; Figure S8: XRD patterns of bare, 2AL, and 2AL-A NCM622 cathodes before cycling (the blue arrows indicate diffraction peaks at 2theta of 37.9° and 38.3°). No obvious difference of crystal structures is observed among bare, 2AL, and 2AL-A NCM622 cathodes before cycling; Table S1: Cycling stability of NCM622 cathodes at 1 C in this study compared to literature reports.

Author Contributions: Conceptualization, J.L.; methodology, J.L.; formal analysis, J.L., X.L. and R.C.; investigation, J.L., J.X. and Y.T.; writing—original draft preparation, J.L.; writing—review and editing, X.L. and R.C.; visualization, G.Y. and H.S.; supervision, X.L., B.S. and R.C. All authors have read and agreed to the published version of the manuscript.

Funding: This work was supported by the National Natural Science Foundation of China (Grant No. 51835005, 51911540476, 51801067 and 52171209), the National Key Research and Development Program of China (Grant No. 2020YFB2010401), Fundamental Research Funds for the Central Universities, HUST (Grant No. 2019kfyXMBZ025 and 2020kfyXJJS100), Program for HUST Academic Frontier Youth Team (Grant No. 2018QYTD03) and Tencent foundation.

Institutional Review Board Statement: Not applicable.

Informed Consent Statement: Not applicable.

Data Availability Statement: Data sharing is not applicable to this article.

Acknowledgments: We would also like to acknowledge the technology supports from the Analytic Testing Center and Flexible Electronics Research Center of HUST.

Conflicts of Interest: The authors declare no conflict of interest.

References

1. Ryu, H.-H.; Park, K.-J.; Yoon, C.S.; Sun, Y.-K. Capacity fading of Ni-rich $LiNi_xCo_yMn_{1-x-y}O_2$ ($0.6 \leq x \leq 0.95$) cathodes for high-energy-density lithium-ion batteries: Bulk or surface degradation? *Chem. Mater.* **2018**, *30*, 1155–1163. [CrossRef]
2. Xu, C.; Guan, S.Q.; Li, L.X.; Sun, C.G.; An, B.G.; Geng, X. Electrochemical properties of $LiNi_{0.6}Co_{0.2}Mn_{0.2}O_2$ cathode materials prepared with different ammonia content. *Coatings* **2021**, *11*, 932. [CrossRef]
3. Noh, H.-J.; Youn, S.; Yoon, C.S.; Sun, Y.-K. Comparison of the structural and electrochemical properties of layered $LiNi_xCo_yMn_zO_2$ (x = 1/3, 0.5, 0.6, 0.7, 0.8 and 0.85) cathode material for lithium-ion batteries. *J. Power Sources* **2013**, *233*, 121–130. [CrossRef]
4. Liu, H.; Wolf, M.; Karki, K.; Yu, Y.-S.; Stach, E.A.; Cabana, J.; Chapman, K.W.; Chupas, P.J. Intergranular cracking as a major cause of long-term capacity fading of layered cathodes. *Nano Lett.* **2017**, *17*, 3452–3457. [CrossRef]
5. Jung, R.; Linsenmann, F.; Thomas, R.; Wandt, J.; Solchenbach, S.; Maglia, F.; Stinner, C.; Tromp, M.; Gasteiger, H.A. Nickel, manganese, and cobalt dissolution from Ni-rich NMC and their effects on NMC622-graphite cell. *J. Electrochem. Soc.* **2019**, *166*, A378–A389. [CrossRef]
6. Hatsukade, T.; Schiele, A.; Hartmann, P.; Brezesinski, T.; Janek, J. Origin of carbon dioxide evolved during cycling of nickel-rich layered ncm cathodes. *ACS Appl. Mater. Interfaces* **2018**, *10*, 38892–38899. [CrossRef] [PubMed]
7. Xiong, X.; Wang, Z.; Yue, P.; Guo, H.; Wu, F.; Wang, J.; Li, X. Washing effects on electrochemical performance and storage characteristics of $LiNi_{0.8}Co_{0.1}Mn_{0.1}O_2$ as cathode material for lithium-ion batteries. *J. Power Sources* **2013**, *222*, 318–325. [CrossRef]
8. Chen, A.; Wang, K.; Li, J.; Mao, Q.; Xiao, Z.; Zhu, D.; Wang, G.; Liao, P.; He, J.; You, Y.; et al. The formation, detriment and solution of residual lithium compounds on Ni-Rich layered oxides in lithium-ion batteries. *Front. Energy Res.* **2020**, *8*, 593009–593024. [CrossRef]

9. Cho, D.-H.; Jo, C.-H.; Cho, W.; Kim, Y.-J.; Yashiro, H.; Sun, Y.-K.; Myung, S.-T. Effect of residual lithium compounds on layer Ni-rich Li[$Ni_{0.7}Mn_{0.3}$]O_2. *J. Electrochem. Soc.* **2014**, *161*, A920–A926. [CrossRef]
10. Faenza, N.V.; Bruce, L.; Lebens-Higgins, Z.W.; Plitz, I.; Pereira, N.; Piper, L.F.J.; Amatucci, G.G. Editors' choice—Growth of ambient induced surface impurity species on layered positive electrode materials and impact on electrochemical performance. *J. Electrochem. Soc.* **2017**, *164*, A3727–A3741. [CrossRef]
11. Martinez, A.C.; Grugeon, S.; Cailleu, D.; Courty, M.; Tran-Van, P.; Delobel, B.; Laruelle, S. High reactivity of the nickel-rich $LiNi_{1\text{-}x\text{-}y}Mn_xCo_yO_2$ layered materials surface towards H_2O/CO_2 atmosphere and $LiPF_6$-based electrolyte. *J. Power Sources* **2020**, *468*, 228204–228213. [CrossRef]
12. Arai, H.; Okada, S.; Ohtsuka, H.; Ichimura, M.; Yamaki, J. Characterization and cathode performance of $Li_{1-x}Ni_{1+x}O_2$ prepared with the excess lithium method. *Solid State Ion.* **1995**, *80*, 261–269. [CrossRef]
13. Kim, J.; Lee, H.; Cha, H.; Yoon, M.; Park, M.; Cho, J. Prospect and reality of Ni-rich cathode for commercialization. *Adv. Energy Mater.* **2018**, *8*, 1702028–1702052. [CrossRef]
14. Pritzl, D.; Teufl, T.; Freiberg, A.T.S.; Strehle, B.; Sicklinger, J.; Sommer, H.; Hartmann, P.; Gasteiger, H.A. Editors' choice—Washing of nickel-rich cathode materials for lithium-ion batteries: Towards a mechanistic understanding. *J. Electrochem. Soc.* **2019**, *166*, A4056–A4066. [CrossRef]
15. Jo, J.H.; Jo, C.-H.; Yashiro, H.; Kim, S.-J.; Myung, S.-T. Re-heating effect of Ni-rich cathode material on structure and electrochemical properties. *J. Power Sources* **2016**, *313*, 1–8. [CrossRef]
16. Jo, C.-H.; Cho, D.-H.; Noh, H.-J.; Yashiro, H.; Sun, Y.-K.; Myung, S.T. An effective method to reduce residual lithium compounds on Ni-rich Li[$Ni_{0.6}Co_{0.2}Mn_{0.2}$]O_2 active material using a phosphoric acid derived Li_3PO_4 nanolayer. *Nano Res.* **2014**, *8*, 1464–1479. [CrossRef]
17. Wang, W.; Wu, L.; Li, Z.; Huang, K.; Chen, Z.; Lv, C.; Dou, H.; Zhang, X. Stabilization of a 4.7 V High-Voltage Nickel-Rich Layered Oxide Cathode for Lithium-Ion Batteries through Boron-Based Surface Residual Lithium-Tuned Interface Modification Engineering. *Chemelectrochem* **2021**, *8*, 2014–2021. [CrossRef]
18. Zhang, S.S.; Ma, L. Oxalic Acid as a cathode additive increasing rate capability of ni-rich layered cathode materials. *J. Electrochem. Soc.* **2021**, *168*, 080512–080518. [CrossRef]
19. Kim, Y.; Park, H.; Warner, J.H.; Manthiram, A. Unraveling the intricacies of residual lithium in high-Ni cathodes for lithium-ion batteries. *ACS Energy Lett.* **2021**, *6*, 941–948. [CrossRef]
20. Li, Q.; Zhuang, W.; Li, Z.; Wu, S.; Li, N.; Gao, M.; Li, W.; Wang, J.; Lu, S. Realizing superior cycle stability of a Ni-Rich layered $LiNi_{0.83}Co_{0.12}Mn_{0.05}O_2$ cathode with a B_2O_3 surface modification. *ChemElectroChem* **2020**, *7*, 998–1006. [CrossRef]
21. Kim, J.; Lee, J.; Ma, H.; Jeong, H.Y.; Cha, H.; Lee, H.; Yoo, Y.; Park, M.; Cho, J. Controllable solid electrolyte interphase in nickel-rich cathodes by an electrochemical rearrangement for stable lithium-ion batteries. *Adv. Mater.* **2018**, *30*, 1704309–1704317. [CrossRef]
22. Kim, J.; Lee, J.; Bae, C.; Kang, B. Sublimation-induced gas-reacting process for high-energy-density Ni-rich electrode materials. *ACS Appl. Mater. Interfaces* **2020**, *12*, 11745–11752. [CrossRef]
23. Seong, W.M.; Cho, K.H.; Park, J.W.; Park, H.; Eum, D.; Lee, M.H.; Kim, I.S.; Lim, J.; Kang, K. Controlling Residual lithium in high-nickel (>90%) lithium layered oxides for cathodes in lithium-ion batteries. *Angew. Chem. Int. Ed.* **2020**, *59*, 18662–18669. [CrossRef] [PubMed]
24. Li, Z.; Li, J.; Liu, X.; Chen, R. Progress in enhanced fluidization process for particle coating via atomic layer deposition. *Chem. Eng. Process.* **2021**, *159*, 108234. [CrossRef]
25. Cao, K.; Cai, J.; Shan, B.; Chen, R. Surface functionalization on nanoparticles via atomic layer deposition. *Sci. Bull.* **2020**, *65*, 678–688. [CrossRef]
26. Zhao, Y.; Zhang, L.; Liu, J.; Adair, K.; Zhao, F.; Sun, Y.; Wu, T.; Bi, X.; Amine, K.; Lu, J.; et al. Atomic/molecular layer deposition for energy storage and conversion. *Chem. Soc. Rev.* **2021**, *50*, 3889–3956. [CrossRef] [PubMed]
27. Zhu, W.; Huang, X.; Liu, T.; Xie, Z.; Wang, Y.; Tian, K.; Bu, L.; Wang, H.; Gao, L.; Zhao, J. Ultrathin Al_2O_3 coating on $LiNi_{0.8}Co_{0.1}Mn_{0.1}O_2$ cathode material for enhanced cycleability at extended voltage ranges. *Coatings* **2019**, *9*, 92. [CrossRef]
28. Kong, J.-Z.; Wang, S.-S.; Tai, G.-A.; Zhu, L.; Wang, L.-G.; Zhai, H.-F.; Wu, D.; Li, A.-D.; Li, H. Enhanced electrochemical performance of $LiNi_{0.5}Co_{0.2}Mn_{0.3}O_2$ cathode material by ultrathin ZrO_2 coating. *J. Alloys Compd.* **2016**, *657*, 593–600. [CrossRef]
29. Qin, C.; Cao, J.; Chen, J.; Dai, G.; Wu, T.; Chen, Y.; Tang, Y.; Li, A.; Chen, Y. Improvement of electrochemical performance of nickel rich $LiNi_{0.6}Co_{0.2}Mn_{0.2}O_2$ cathode active material by ultrathin TiO_2 coating. *Dalton Trans.* **2016**, *45*, 9669–9675. [CrossRef]
30. Kong, J.-Z.; Ren, C.; Tai, G.-A.; Zhang, X.; Li, A.-D.; Wu, D.; Li, H.; Zhou, F. Ultrathin ZnO coating for improved electrochemical performance of $LiNi_{0.5}Co_{0.2}Mn_{0.3}O_2$ cathode material. *J. Power Sources* **2014**, *266*, 433–439. [CrossRef]
31. Manandhar, K.; Wollmershauser, J.A.; Boercker, J.E.; Feigelson, B.N. Growth per cycle of alumina atomic layer deposition on nano- and micro-powders. *J. Vac. Sci. Technol. A* **2016**, *34*, 021519–021528. [CrossRef]
32. Groner, M.D.; Fabreguette, F.H.; Elam, J.W.; George, S.M. Low-temperature Al_2O_3 atomic layer deposition. *Chem. Mater.* **2004**, *16*, 639–645. [CrossRef]
33. Wank, J.R.; George, S.M.; Weimer, A.W. Coating fine nickel particles with Al_2O_3 Utilizing an atomic layer deposition-fluidized bed reactor (ALD-FBR). *J. Am. Ceram. Soc.* **2004**, *87*, 762–765. [CrossRef]
34. Matero, R.; Rahtu, A.; Ritala, M.; Leskelä, M.; Sajavaara, T. Effect of water dose on the atomic layer deposition rate of oxide thin films. *Thin Solid Film.* **2000**, *368*, 1–7. [CrossRef]

35. Jackson, D.H.K.; Kuech, T.F. Electrochemical effects of annealing on atomic layer deposited Al_2O_3 coatings on $LiNi_{0.5}Mn_{0.3}Co_{0.2}O_2$. *J. Power Sources* **2017**, *365*, 61–67. [CrossRef]
36. Gao, Y.; Park, J.; Liang, X. Comprehensive Study of Al- and Zr-modified $LiNi_{0.8}Mn_{0.1}Co_{0.1}O_2$ through synergy of coating and doping. *ACS Appl. Energy Mater.* **2020**, *3*, 8978–8987. [CrossRef]
37. Tang, W.J.; Chen, Z.X.; Xiong, F.; Chen, F.; Huang, C.; Gao, Q.; Wang, T.Z.; Yang, Z.H.; Zhang, W.X. An effective etching-induced coating strategy to shield $LiNi_{0.8}Co_{0.1}Mn_{0.1}O_2$ electrode materials by $LiAlO_2$. *J. Power Sources* **2019**, *412*, 246–254. [CrossRef]
38. Liu, S.; Dang, Z.; Liu, D.; Zhang, C.; Huang, T.; Yu, A. Comparative studies of zirconium doping and coating on $LiNi_{0.6}Co_{0.2}Mn_{0.2}O_2$ cathode material at elevated temperatures. *J. Power Sources* **2018**, *396*, 288–296. [CrossRef]
39. Tatara, R.; Karayaylali, P.; Yu, Y.; Zhang, Y.R.; Giordano, L.; Maglia, F.; Jung, R.; Schmidt, J.P.; Lund, I.; Shao-Horn, Y. The effect of electrode-electrolyte interface on the electrochemical impedance spectra for positive electrode in Li-ion battery. *J. Electrochem. Soc.* **2018**, *166*, A5090–A5098. [CrossRef]
40. Wood, K.N.; Teeter, G. XPS on Li-battery-related compounds: Analysis of inorganic sei phases and a methodology for charge correction. *ACS Appl. Energy Mater.* **2018**, *1*, 4493–4504. [CrossRef]
41. Yao, K.P.C.; Kwabi, D.G.; Quinlan, R.A.; Mansour, A.N.; Grimaud, A.; Lee, Y.-L.; Lu, Y.-C.; Shao-Horn, Y. Thermal stability of Li_2O_2 and Li_2O for Li-air batteries: In situ XRD and XPS studies. *J. Electrochem. Soc.* **2013**, *160*, A824–A831. [CrossRef]
42. Chen, L.; Connell, J.G.; Nie, A.; Huang, Z.; Zavadil, K.R.; Klavetter, K.C.; Yuan, Y.; Sharifi-Asl, S.; Shahbazian-Yassar, R.; Libera, J.A.; et al. Lithium metal protected by atomic layer deposition metal oxide for high performance anodes. *J. Mater. Chem. A* **2017**, *5*, 12297–12309. [CrossRef]
43. Hoskins, A.L.; McNeary, W.W.; Millican, S.L.; Gossett, T.A.; Lai, A.; Gao, Y.; Liang, X.; Musgrave, C.B.; Weimer, A.W. Nonuniform growth of sub-2 nanometer atomic layer deposited alumina films on lithium nickel manganese cobalt oxide cathode battery materials. *ACS Appl. Nano Mater.* **2019**, *2*, 6989–6997. [CrossRef]
44. Huang, X.; Zhang, P.; Liu, Z.; Ma, B.; Zhou, Y.; Tian, X. Fluorine doping induced crystal space change and performance improvement of single crystalline $LiNi_{0.6}Co_{0.2}Mn_{0.2}O_2$ layered cathode materials. *ChemElectroChem* **2021**, *8*, e202100756. [CrossRef]
45. Feng, Z.; Zhang, S.; Rajagopalan, R.; Huang, X.; Ren, Y.; Sun, D.; Wang, H.; Tang, Y. Dual-element-modified single-crystal $LiNi_{0.6}Co_{0.2}Mn_{0.2}O_2$ as a highly stable cathode for lithium-ion batteries. *ACS Appl. Mater. Interfaces* **2021**, *13*, 43039–43050. [CrossRef]
46. Bao, W.; Qian, G.; Zhao, L.; Yu, Y.; Su, L.; Cai, X.; Zhao, H.; Zuo, Y.; Zhang, Y.; Li, H.; et al. Simultaneous enhancement of interfacial stability and kinetics of single-crystal $LiNi_{0.6}Mn_{0.2}Co_{0.2}O_2$ through optimized surface coating and doping. *Nano Lett.* **2020**, *20*, 8832–8840. [CrossRef]
47. Xu, S.; Jing, N.; Hao, H.; Wang, M.; Wang, Z.; Yang, L.; Wang, G.; Chen, J.; Wang, G. Enhanced electrochemical performance of $LiNi_{0.6}Co_{0.2}Mn_{0.2}O_2$ by a negative-thermal-expansion material at elevated temperature. *Energy Technol.* **2021**, *9*, 2100183. [CrossRef]
48. Huang, B.; Yang, X.; Xu, G.; Wang, M.; Gu, Y. Boron-doped single crystal $LiNi_{0.6}Mn_{0.2}Co_{0.2}O_2$ with improved electrochemical performance for lithium-ion batteries. *Ionics* **2019**, *25*, 5819–5827. [CrossRef]
49. Li, G.; You, L.; Wen, Y.; Zhang, C.; Huang, B.; Chu, B.; Wu, J.H.; Huang, T.; Yu, A. Ultrathin Li-Si-O coating layer to stabilize the surface structure and prolong the cycling life of single-crystal $LiNi_{0.6}Co_{0.2}Mn_{0.2}O_2$ cathode materials at 4.5 V. *ACS Appl. Mater. Interfaces* **2021**, *13*, 10952–10963. [CrossRef]
50. Liu, W.; Li, X.; Xiong, D.; Hao, Y.; Li, J.; Kou, H.; Yan, B.; Li, D.; Lu, S.; Koo, A.; et al. Significantly improving cycling performance of cathodes in lithium ion batteries: The effect of Al_2O_3 and $LiAlO_2$ coatings on $LiNi_{0.6}Co_{0.2}Mn_{0.2}O_2$. *Nano Energy* **2018**, *44*, 111–120. [CrossRef]
51. Li, X.; Liu, J.; Banis, M.N.; Lushington, A.; Li, R.; Cai, M.; Sun, X. Atomic layer deposition of solid-state electrolyte coated cathode materials with superior high-voltage cycling behavior for lithium ion battery application. *Energy Environ. Sci.* **2014**, *7*, 768–778. [CrossRef]